NDT and E International 91 (2017) 79–87

Contents lists available at ScienceDirect

NDT and E International

journal homepage: www.elsevier.com/locate/ndteint

Local-stress-induced thermal conductivity anisotropy analysis using non-destructive photo-thermo-mechanical lock-in thermography (PTM-LIT) imaging

Huiting Huan [a,b], Andreas Mandelis [a,b,*], Lixian Liu [a,b], Alexander Melnikov [b]

[a] School of Optoelectronic Information, University of Electronic Science and Technology of China, Chengdu, 610054, China
[b] Center for Advanced Diffusion-Wave and Photoacoustic Technologies (CADIPT), Department of Mechanical and Industrial Engineering, University of Toronto, Toronto, ON, M5S 3G8, Canada

ARTICLE INFO

Keywords:
Anisotropic thermal conductivity
Non-destructive imaging
Isothermal contour
Photo-thermo-mechanical lock-in thermography (PTM-LIT)

ABSTRACT

When tensile loading is exerted on a sample, internal stress will be generated to counterbalance the external force. The accumulation of local stress results in the change of thermal properties and the sample becomes locally anisotropic, wherein lies the significance of correlation between mechanical properties and thermal parameters. In this research, anisotropic thermal conductivity was considered as the direct result of tensile loading and was interpreted by a theoretical three-dimensional anisotropic diffusion-wave model. Photo-thermo-mechanical lock-in thermography (PTM-LIT) was introduced and used with a focused laser beam and a mid-infrared camera viewing an aluminum alloy sample fixed on a dynamic home-made tensile rig. A numerical two-dimensional Fourier transform was used to compute the thermal-wave field and the effects of several important factors were investigated. Both theoretical and experimental images were analyzed with an isothermal conductivity anisotropy contour fitting approach. It was demonstrated that PTM-LIT can qualitatively and quantitatively reveal otherwise hard-to- measure mechanical property behavior of materials subjected to tensile loading from the stress-free state to its ultimate level of mechanical strength before fracture.

1. Introduction

As modern-day manufacturing industry is increasingly required to handle ever more complicated structural parts, delicate non-destructive testing/imaging (NDT/NDI) methods become necessary to evaluate the quality and properties of these products. Mechanical performance is a very important aspect of quality control that affects the stability and durability of materials [1]. There are many conventional NDT/NDI approaches including X-rays, ultrasonic scans, eddy currents etc. [2]. More recently, the laser induced photo-thermal-mechanical radiometry (PTMR) technique was proven to be capable of monitoring the mechanical condition of solids in terms of thermal conductivity changes [3–6]. Unlike laser ultrasonic testing which intrinsically involves both thermal and elastic wave fields, PTMR only focuses on thermal parameters through the detection of mid-infrared emission and thus simplifies both experimental procedure and theoretical analysis. The advent of mid-infrared cameras used in laser heating lock-in thermography (LIT) has further boosted its industrial on-line applications through the emergence of totally non-contact and non-destructive imaging [7,8]. Based on our previous development of PTMR, this work further extends the methodology to photo-thermo-mechanical lock-in thermography (PTM-LIT) imaging as a next generation NDI technique. It was implemented with a focused laser beam and a mid-infrared camera dynamically recording the thermal-wave field at the front surface of the sample. An anisotropic thermal-wave theory was derived and used to analyze the mechanically-induced thermal conductivity anisotropy and the experimental images were quantified by means of isothermal contour fittings.

2. Experimental

The experimental system is shown in Fig. 1. A general aircraft aluminum 6061 alloy sample (density: 2700 kg/m^3, thermal conductivity: 155 W/m·K, heat capacity: 896 J/kg·K) was machined into a “dog-bone” shape with 2-mm thickness at the center and was fixed on the two clamps of a flexible tensile rig. The local strain was monitored at its tapered middle (waist) using an adhesive foil strain gauge (KYOWA®,

* Corresponding author. Center for Advanced Diffusion-Wave and Photoacoustic Technologies (CADIPT), Department of Mechanical and Industrial Engineering, University of Toronto, Toronto, ON, M5S 3G8, Canada.
E-mail address: mandelis@mie.utoronto.ca (A. Mandelis).

http://dx.doi.org/10.1016/j.ndteint.2017.06.008
Received 12 December 2016; Received in revised form 22 February 2017; Accepted 23 June 2017
Available online 26 June 2017
0963-8695/© 2017 Elsevier Ltd. All rights reserved.

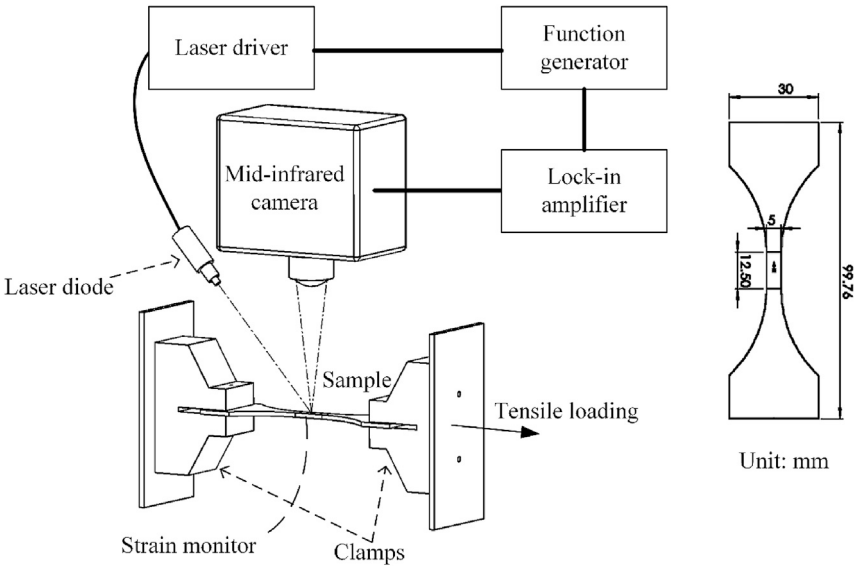

Fig. 1. The schematic of the PTM-LIT imaging system.

sensitivity: 10^{-6}). A high power focused diode laser (808 nm, 7.7 W, 0.5-mm beam diameter) generated thermal waves inside the sample, and LIT images were captured by the mid-infrared camera (128 × 164 pixels, 1 pixel ≈ 0.04 × 0.04 mm^2, lens: 67-mm diameter and 80-mm focal length). The camera had an optical window of 8–12 μm and no sensitivity to scattered laser radiation due to the oblique incidence of the laser beam. During the tests, uniaxial tensile loading was applied via the clamps and gradually increased while several groups of images were obtained at specific strain readings. Unlike earlier work [7] which focused on measuring the residual stress in metals already fractured, in this research the evolution of the entire mechanical history of the sample was recorded in terms of PTM-LIT images vs. strain from the stress-free condition up to the fracture point.

3. Anisotropic thermal-wave theory and isothermal contours

The connection between stress and thermal conductivity was theoretically derived by Landau et al. who established that thermal properties of solids become anisotropic and change with the local stress tensor [9]. The behavior of anisotropic thermal conduction and diffusion was theoretically investigated with the aid of integral transforms by Iravani et al. [10] and experimentally verified with the beam deflection technique on polymers [11–13]. In agreement with the sample and frequencies we used, a laterally semi-infinite plate of finite thickness is considered in this model and effects of the lateral boundaries are neglected [14–16]. The major advantage of this theoretical model is the absence of cross-terms in the thermal-wave equation.

The generalized form of the thermal diffusion equation in anisotropic materials is given by Refs. [3,9]:

$$\rho C\frac{\partial T}{\partial t} - \nabla_i\cdot\left(k_{ij}\cdot\nabla_j T\right) = g \tag{1}$$

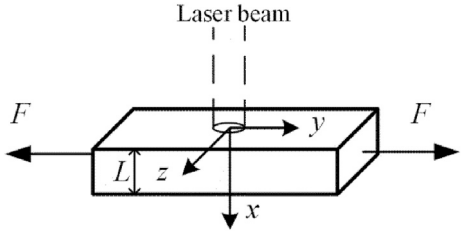

Fig. 2. Local coordinate system for theoretical PTM-LIT analysis.

k_{ij}, $i, j = x, y$ or z is the anisotropic thermal conductivity tensor of order 2 which is symmetric, i.e. $k_{ij} = k_{ji}$ for $i \neq j$. $\nabla_i = \partial/\partial x_i$ is the gradient operator with respect to spatial coordinate i; g is the heat source term. ρ, C are density and specific heat capacity, respectively, and are considered constant under tensile loading conditions [17]. Expanding Eq. (1) in Cartesian coordinates (as shown in Fig. 2) [18] and converting to frequency domain for harmonic excitation ($\omega = 2\pi f$) yields

$$i\omega\rho CT(x,y,z;\omega) = k_{xx}\frac{\partial^2 T}{\partial x^2} + k_{yy}\frac{\partial^2 T}{\partial y^2} + k_{zz}\frac{\partial^2 T}{\partial z^2} + 2k_{xy}\frac{\partial^2 T}{\partial x\partial y} + 2k_{xz}\frac{\partial^2 T}{\partial x\partial z} + 2k_{yz}\frac{\partial^2 T}{\partial y\partial z} + g \tag{2}$$

Because anisotropy is the result of local stress, it is assumed that the thermal conductivity tensor is a function of the local stress tensor, τ_{ij}, which is virtually diagonal under uniaxial loading. Thus, the non-diagonal terms vanish and the conductivity tensor components are solely related to their corresponding local stresses: k_{ii} (τ_{ii}). By introducing the new coordinate system (Appendix)

$$X = x, Y = \sqrt{k_{xx}/k_{yy}}y, Z = \sqrt{k_{xx}/k_{zz}}z \tag{3}$$

equation (2) can be rewritten in a renormalized form as:

$$\frac{i\omega\rho CT(x,y,z,\omega)}{k_{xx}} = \frac{\partial^2 T}{\partial X^2} + \frac{\partial^2 T}{\partial Y^2} + \frac{\partial^2 T}{\partial Z^2} \tag{4}$$

in the absence of a heat source. For laser induced heating, the thin plate $0 \le x \le L$ is subject to the following flux boundary conditions:

$$-k_{xx}\left.\frac{\partial T}{\partial X}\right|_{X=0} = \frac{\beta I_0}{\pi r_0^2}\exp\left[-\frac{k_{xx}}{r_0^2}\left(\frac{Y^2}{k_{yy}} + \frac{Z^2}{k_{zz}}\right)\right] \tag{5a}$$

$$-k_{xx}\left.\frac{\partial T}{\partial X}\right|_{X=L} = 0 \tag{5b}$$

where r_0 is the Gaussian radius of the laser beam, β is the non-radiative energy conversion coefficient and I_0 is the incident laser intensity. It can be seen that the Gaussian beam is reshaped in the new coordinate system if $k_{xx} \neq k_{yy} \neq k_{zz}$ after coordinate renormalization. The diffusion equation has no cross terms in the new coordinate system while the first boundary condition (5a) breaks its azimuthal symmetry. Equations (4) and (5) can

be solved either by Green function methods [19] or by an integral transformation [6] in Cartesian coordinates. Both approaches require numerical computation. Applying a 2-D Fourier transformation with respect to coordinates Y and Z, the solution in the Fourier domain is represented in the following form:

$$\tilde{T} = Ae^{-sX} + Be^{sX}$$
$$s(\xi,\eta,\omega) = \sqrt{\xi^2+\eta^2+i\omega\rho C/k_{xx}} \tag{6a}$$

$$\tilde{T}(X,\xi,\eta,\omega) = \int_{-\infty}^{\infty}\int_{-\infty}^{\infty} T(X,Y,Z,\omega)\exp(-i\xi Y - i\eta Z)dYdZ \tag{6b}$$

A, B are coefficients describing, respectively, forward and back-propagated thermal waves along the thickness direction. The boundary condition at the front surface now becomes:

$$-k_{xx}\left.\frac{\partial\tilde{T}}{\partial X}\right|_{X=0} = \frac{\beta I_0}{r_0^2\sqrt{\kappa_1\kappa_2}}\exp\left[-\frac{1}{4}\left(\frac{\xi^2}{\kappa_1}+\frac{\eta^2}{\kappa_2}\right)\right]$$
$$\kappa_1 = \frac{k_{xx}}{k_{yy}r_0^2}, \kappa_2 = \frac{k_{xx}}{k_{zz}r_0^2} \tag{7}$$

The thermal-wave distribution at the front surface, the field captured by the camera by means of infrared thermal photon emissions, is derived from the inverse 2-D Fourier transform in Fourier space (ξ, η):

$$T(0,y,z;\omega) = \frac{1}{(2\pi)^2}\int_{-\infty}^{\infty}\int_{-\infty}^{\infty}\tilde{T}(0,\xi,\eta;\omega)\exp\left(i\sqrt{k_{xx}/k_{yy}}\,\xi y + i\sqrt{k_{xx}/k_{zz}}\,\eta z\right)d\xi d\eta \tag{8a}$$

$$\tilde{T}(0,\xi,\eta;\omega) = A + B = \frac{I_0\sqrt{k_{yy}k_{zz}}}{k_{xx}^2 s(\xi,\eta,\omega)}\left(\frac{1+e^{-2sL}}{1-e^{-2sL}}\right)\exp\left[-\frac{1}{4}\left(\frac{k_{yy}r_0^2}{k_{xx}}\xi^2+\frac{k_{zz}r_0^2}{k_{xx}}\eta^2\right)\right] \tag{8b}$$

It should be noted that Eq. (8a) is a function of the original local coordinates (x, y) of the material. By numerical calculation, the amplitude and phase images are shown in Fig. 3 as isothermal contours.

The shape and features of these contours can be further quantified by fitting the data to the equation of an ellipse. As the external loading is pure tension without torque, no rotational asymmetry is introduced to the contours. The two axes of the ellipse are still paralleled to y- and z-axes which can be expressed in ellipsoidal coordinates as:

$$\begin{cases} y = a\cos\theta + y_0 \\ z = b\sin\theta + z_0 \end{cases}, 0 \le \theta \le 2\pi \text{ or } \frac{(y-y_0)^2}{a^2}+\frac{(z-z_0)^2}{b^2} = 1 \tag{9}$$

a/b is the major/minor axis length along the y-/z-direction; y_0 and z_0 are the center coordinates for the elliptic contours. These four parameters completely specify the behavior of elliptical (anisotropic) diffusion-waves due to local stresses. To clearly show the change of a and b under stress, we introduce the ratios of axis lengths as: $R_a = a_1/a_0$ and $R_b = b_1/b_0$. The subscripts 1 and 0 indicate axis lengths at the loaded and load-free (reference) state, respectively. By computing axis ratios, the SNR and contrast of thermal diffusion with respect to the reference state can be effectively enhanced.

4. Results and discussion

One group of experimental PTM-LIT images is shown in Fig. 4. The amplitude contours are heavily distorted and hard to maintain patterned shapes because they are sensitive to random surface nonuniformities (dust, scratches, reflectivity variations, etc.). In comparison, the phase signals show higher regularity and are thus regarded to be more suitable for quantitative contour elliptical fitting.

4.1. Analysis of optical and material parameters with anisotropic thermal waves

The impact of several optical and material parameters was investigated in the theoretical analysis.

1) *Conductivity tensor component change:* According to the anisotropic thermal-wave theory, the three components of the conductivity tensor coincide with the three principal axes x, y and z. It is assumed that the thermal conductivity components change in a linear manner:

$$k_{ii} = k_0(1+P_{ii}), i = x,y,z; P_{ii} = f(\tau_{ii}) \tag{10}$$

P_{ii} is the percentage of thermal conductivity change and τ_{ii} is the local stress tensor. Furthermore, by fitting the phase contours from the computed images to an elliptic equation, the effect of the thermal

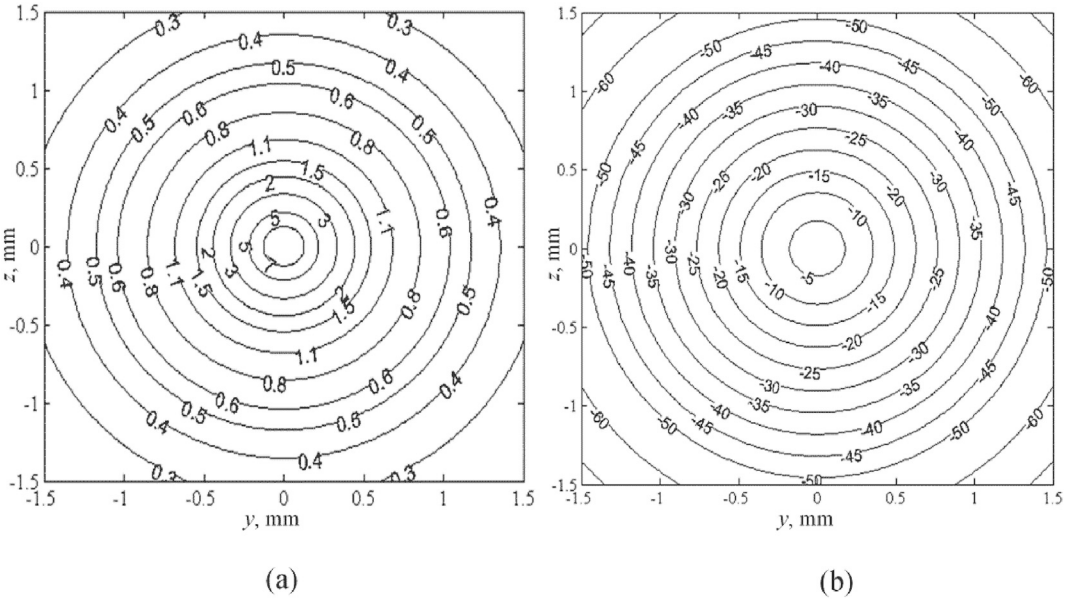

Fig. 3. **(a)** Amplitude (unit: a.u.) and **(b)** phase (unit: degree) isothermal contours at the front surface ($x = 0$) computed from Eq. (8a) (thermal properties of aluminum 6061 was adopted) at 5 Hz using $r_0 = 0.2$ mm and isotropic, $k_{xx} = k_{yy} = k_{zz}$.

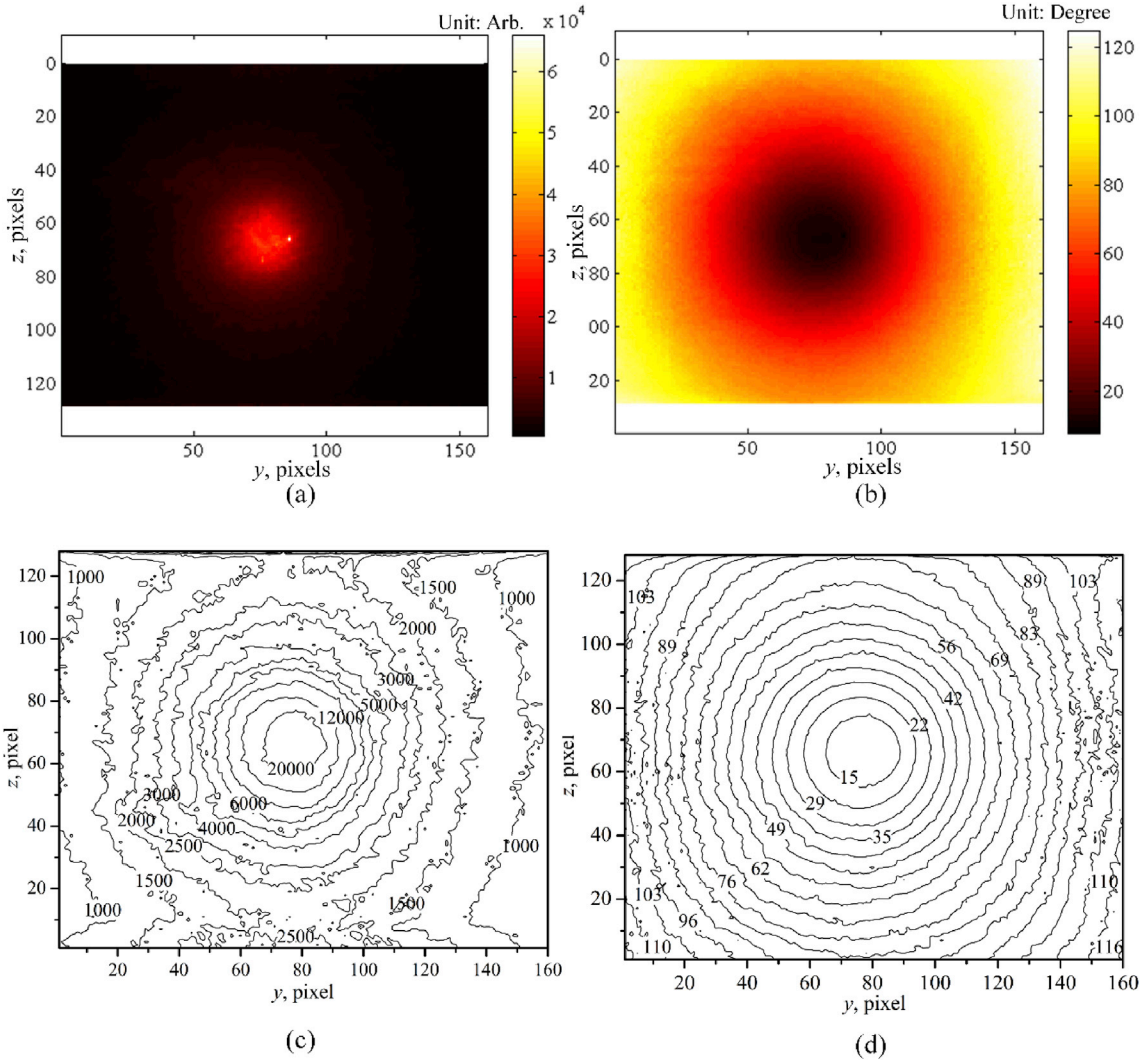

Fig. 4. Experimental PTM-LIT images on the "dog-bone" sample: **(a)** amplitude image (unit: a.u.); **(b)** phase lag image (unit: degree); **(c)** amplitude isothermal contours; **(d)** phase lag isothermal contours; (1 pixel ≈ 0.04 mm, 5 Hz, load-free).

conductivity change on the phase contours is shown in Fig. 5(a). The thermal-wave model assumes infinite lateral (y,z) extent, therefore, k_{yy} and k_{zz} are equivalent and have the same effect on the phase profile (continuous lines only), For directions parallel to the upper surface (y-z plane), the increasing conductivity tensor component only results in axis "elongation" along its corresponding direction (a for k_{yy} and b for k_{zz}). Along the thickness direction (x-axis), increasing conductivity leads to "compression" of both elliptic axes which change by the same ratio. The dashed curves show the change of R_a and R_b as a result of changes in the two conductivity tensor components (k_{yy} and k_{xx}). When $P_{xx} = \pm 0.02$, the R_a and R_b dependence on P_{yy} still exhibits linear pattern parallels to the solid curves, only with a displacement that is equal to the portion contributed from k_{xx} change. This relation indicates that the three components P_{xx}, P_{yy} and P_{zz} make linear contributions independent of each other to changes in R_a and R_b. Consequently, the linear correlation can be further expressed as:

$$\begin{aligned} R_a &= n_1 P_{yy} + n_2 P_{xx} + 1 \\ R_b &= n_1 P_{zz} + n_2 P_{xx} + 1 \end{aligned} \tag{11a}$$

n_1, n_2 are defined as

$$n_1 = \frac{dR_a}{dP_{yy}} = \frac{dR_b}{dP_{zz}}, n_2 = \frac{dR_a}{dP_{xx}} = \frac{dR_b}{dP_{xx}} \tag{11b}$$

Using a linear best-fit of the 30° phase lag contour in Fig. 3(b) yields $n_1 \approx 0.54$, $n_2 \approx -0.27$ as the slopes of the corresponding curves. Equation (11a) clearly shows that the independent change of thermal conductivity tensor components contributes to the elongation or compression of the ellipse in a linear manner. A more useful criterion for the thermal conductivity anisotropy is:

$$\lambda = \frac{R_a - 1}{R_b - 1} = \frac{P_{yy} + nP_{xx}}{P_{zz} + nP_{xx}} \tag{12}$$

where $n = n_2/n_1$ and $-1 < n < 0$. λ is the ratio of the relative change of the elliptic axes ratio (R_a and R_b) and is directly obtained by means of elliptical fitting. This parameter involves the three tensor components and constructs numerator and denominator by equally projecting P_{xx} onto the y- and z-axes respectively. The value of λ acts as a thermal conductivity anisotropy indicator and directly specifies the thermal conductivity anisotropy condition as shown in Table 1. That Table shows symmetric features with respect to P_{yy} and P_{zz} since they are interchangeable in the laterally infinite diffusion-wave model. Isotropic diffusion occurs when either all conductivity components remain the same ($\lambda = 0$, reference state) or they change by the same amount ($\lambda = 1$). Laterally uniform diffusion occurs if k_{yy} and k_{zz} change by the same amount. When only one lateral directional component (k_{yy} or k_{zz}) changes, thermal anisotropy emerges and either the numerator or the

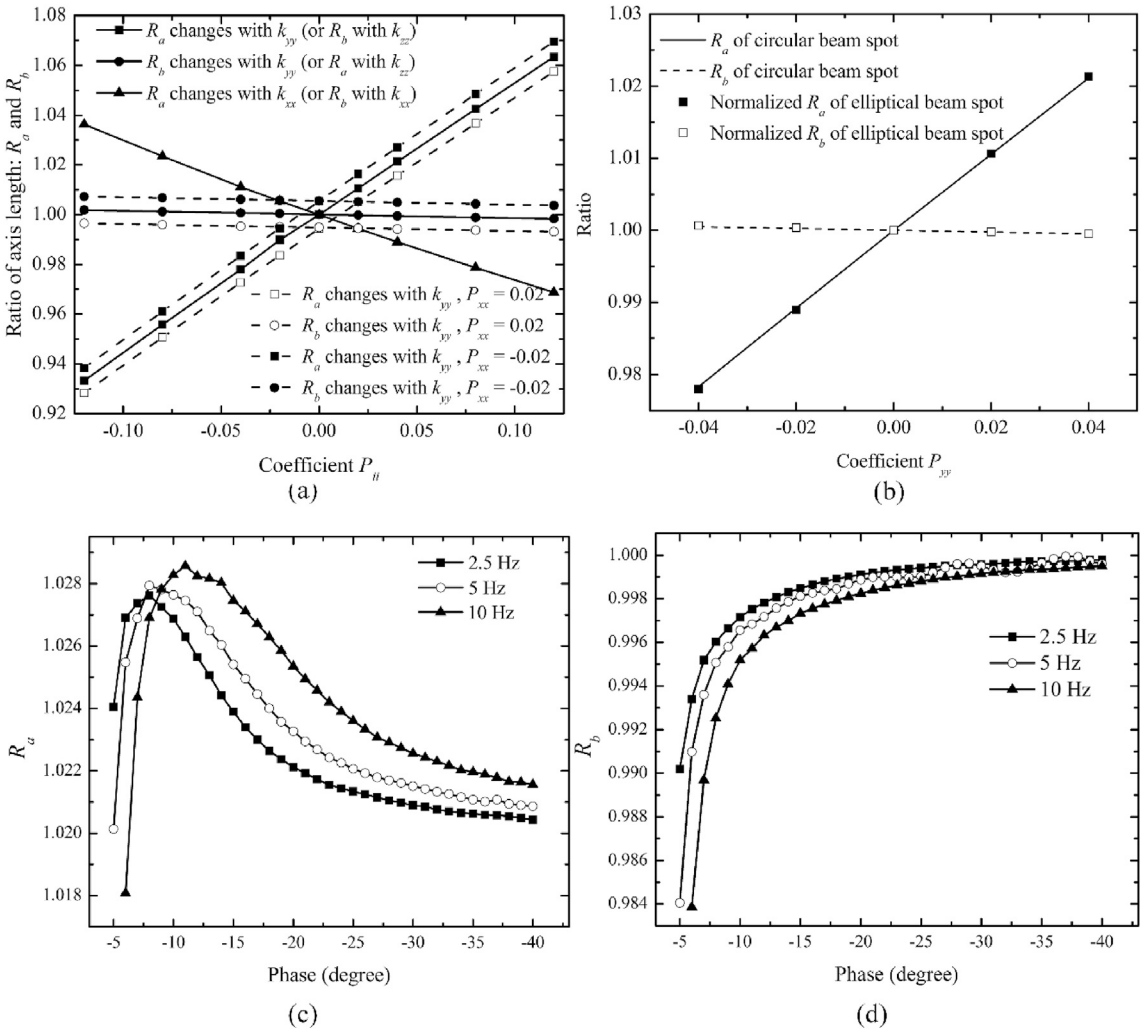

Fig. 5. **(a)** Influence of thermal conductivity tensor change on the phase contour ellipses (−30° phase contour); **(b)** The effectiveness of normalization in compensating for contour distortion due to obliqueness (angle of incidence for elliptic beam spot: 22.7°, r_0 = 0.2 mm, 5 Hz); **(c)** R_a and **(d)** R_b between changed and unchanged state for phase contours at three frequencies (k_{yy} increases 4%, P_{yy} = 0.04).

denominator of λ becomes zero ($\lambda = 0$, $\lambda = \infty$); For all other λ cases, only the relative quantitative relation between the two lateral directional conductivities can be obtained within the range of thermal-wave anisotropy.

2) *Obliqueness:* When a Gaussian laser beam is incident at an angle θ to a plane surface, the intersection contours become elliptic. The isothermal contours of the phase image also becomes elliptical even without loading. An effective way to compensate for the effect of non-circular laser spot is selecting suitable theoretical elliptical best fits to the obliqueness-generated non-circular thermal-wave contours. This helps quantify the two axes of the elliptical contours under the unstressed condition so as to normalize out this effect from further, mechanical-stress-related, elliptic contour changes. The effectiveness and performance of the normalization is shown in Fig. 5(b). It is clear that after normalization to the reference state, the obliquely incident beam induced ellipticity can be canceled out.
3) *Contour location and frequency:* It is worth noting that the effect of thermal conductivity changes on phase contours also varies with distance from the beam center. As shown in Fig. 5(c) and (d), the axis length ratios between anisotropic and isotropic states are functions of distance (resulting in different phase lags). Being close to the beam center (small phase lag), the thermal wave travels faster in the direction of k_{yy} (a increase) and slower in the direction of k_{zz} (b decrease), even though k_{yy} increases only by 4% (k_{zz} remains the same). Away from the center, this effect along the z-coordinate gradually disappears and R_b approaches unity. The magnitude of elongation or compression of the elliptical axes is also a function of frequency: higher frequency limits the extent of the thermal wave and makes the contours more sensitive to conductivity changes.

Table 1
The criterion of the thermal anisotropy indicator for uniformity determination (the symbol "+/−" means positive numerator and negative denominator and so on).

Value of the indicator	Result	Description
$\lambda = 0$	$P_{xx} = P_{yy} = 0$, $P_{zz} \neq 0$	Anisotropic, only k_{zz} changes
	$P_{xx} = P_{yy} = P_{zz} = 0$	Reference state
$\lambda = 1$	$P_{yy} = P_{zz} < 0$	Laterally Isotropic, $k_{yy} = k_{zz} < k_0$
	$P_{yy} = P_{zz} > 0$	Laterally Isotropic, $k_{yy} = k_{zz} > k_0$
	$P_{yy} = P_{zz} = P_{zz} \neq 0$	Isotropic, $k_{yy} = k_{zz} = k_{xx} \neq k_0$
+/+, $\lambda > 1$	$P_{yy} > P_{zz}$	Anisotropic, $k_{yy} > k_{zz}$
−/−, $1 > \lambda > 0$		
+/−, $\lambda < 0$		
+/+, $1 > \lambda > 0$	$P_{yy} < P_{zz}$	Anisotropic, $k_{yy} < k_{zz}$
−/−, $\lambda > 1$		
−/+, $\lambda < 0$		
$\lambda = \infty$	$P_{xx} = P_{zz} = 0$, $P_{yy} \neq 0$	Anisotropic, only k_{yy} changes

4.2. Local stress induced anisotropy: PTM-LIT experimental results

According to the foregoing theoretical analysis, the phase contours chosen for quantifying the elliptical best fits should neither be too close to the focused laser beam incidence location, i.e. with very small phase lag, nor too far away from the center where the signal-to-noise ratio deteriorates. The experimental contours for fitting to the theory were picked from a medium range (30–45° phase lag). Within the elastic regime, the phase lag contours at various frequencies are shown in Fig. 6(a)-(c). At each frequency, the centers of these ellipse contours exhibit a slight rightward translation, as the tensile loading increases with respect to its original position (0 μm/m). This is the result of the obliquely incident beam and Poisson's displacement as interpreted in Fig. 6(d). This displacement effect becomes more obvious with increasing frequency.

The deformation-induced displacement can be eliminated by considering the ratio of elliptic axis lengths (R_a and R_b) only. The best-fit results are shown in Fig. 7(a). In agreement with the theoretical analysis, at high frequencies the contour axis length ratio change is more significant. R_b remains close to 1 which suggests that change in k_{yy} is the predominant factor (P_{xx} and P_{zz} are approx. zero). This trend is in agreement with the local stress feature (τ_{yy} is predominant under uniaxial loading along the y direction) and indicates that the thermal conductivity becomes a tensor and has a monotonic dependence on the local stress tensor. The increasing trend of the R_a suggests that tensile loading accelerates the conduction of heat along the loading direction and stress alone causes ~2% change in thermal conductivity within the elastic regime.

The mechanical performance of the material represented in terms of contour axis length ratios and center location is shown in Fig. 7(b). Within the elastic regime (up to about 3500 μm/m [3]), the center location coordinate y_0 changes in a linear and increasing pattern, the result of elastic deformation and Poisson displacement of the surface along the thickness direction. Moving into the plastic regime in which the linear stress-strain relation becomes invalid [20], the material undergoes permanent and irreversible changes and its thermal conductivity become seriously anisotropic along the orthogonal directions, so the phase contours become more elliptic. Around 13000 μm/m the strain gauge failed because the local strain exceeded its detectable range. For the last several points before fracture, the trend for displacement of the contour center becomes steep, indicating a large deformation at the very end of the material lifetime, a phenomenon referred to as “necking” [21]. The phase

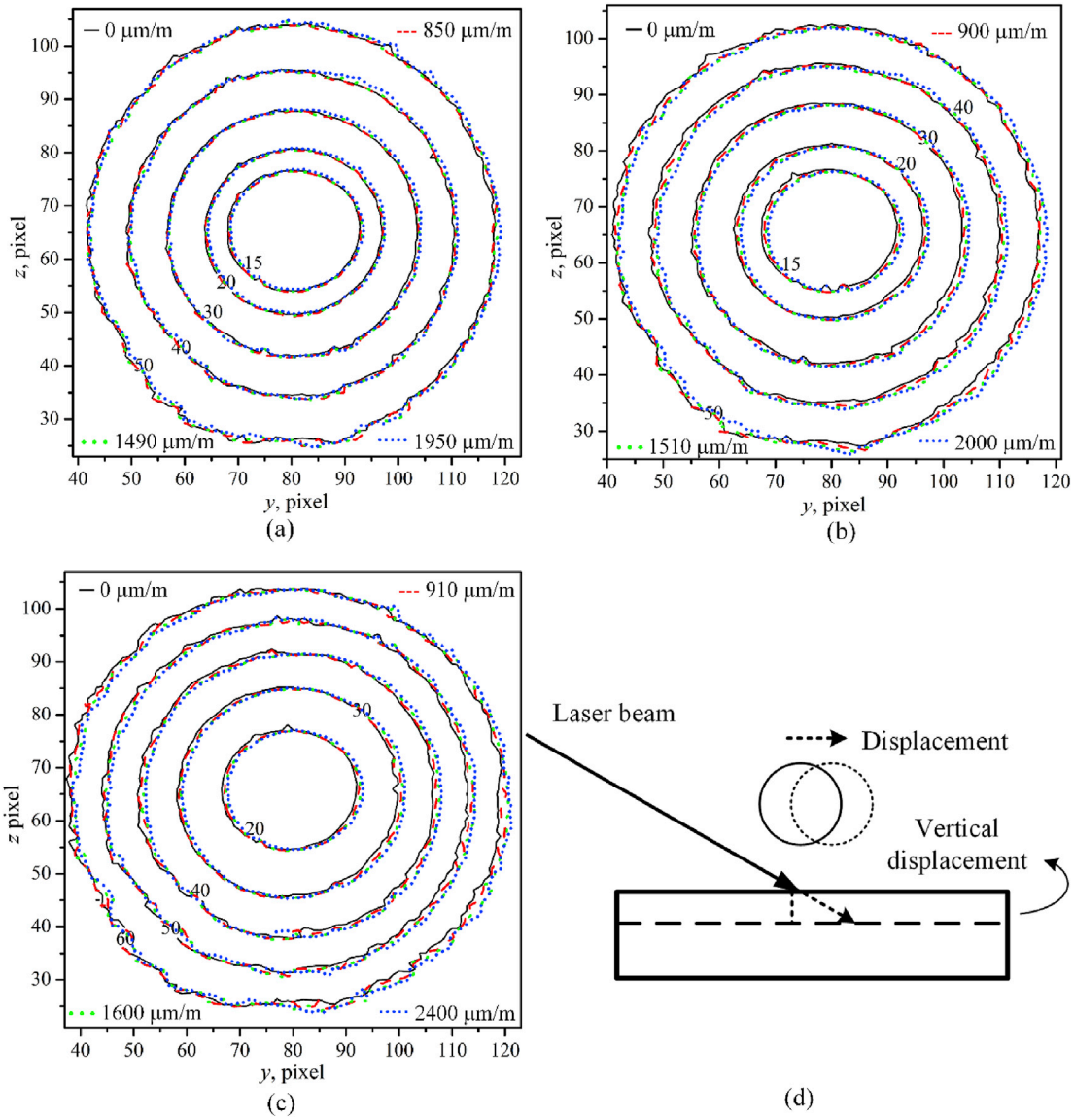

Fig. 6. Phase lag contours at various loads at **(a)** 2 Hz, **(b)** 5 Hz and **(c)** 10 Hz; **(d)** schematic of contour displacement phenomenon.

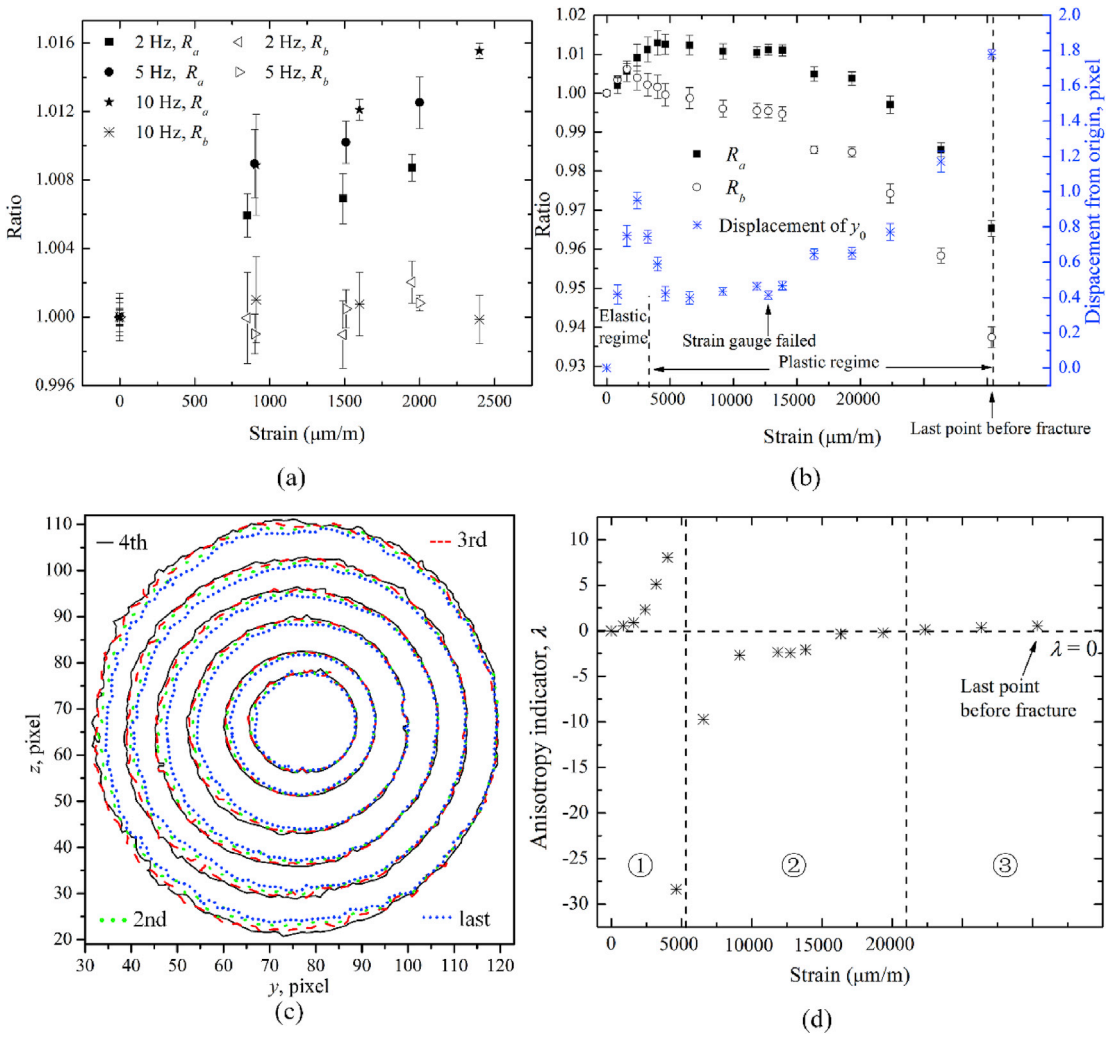

Fig. 7. Contour best fitting results of experimental PTM-LIT images: **(a)** ratios of the two elliptic axis change with strain within the elastic regime (from fitting the 30° phase lag contour); **(b)** ratio of the two axes and center location (y_0 coordinate) change with strain through the entire tensile loading history (from fitting the 40° phase lag contour); **(c)** phase lag contours of the last four points before fracture (order: 4th-3rd-2nd-last point before facture); **(d)** the anisotropy indicator λ changes along the entire loading history.

contours captured at each of the last four states before fracture and under the necking condition are shown in Fig. 7(c). Very drastic shift and deformation of the group of contours are found which implies the instability and fracture-hazard status of the sample. A similar steep feature also occurs with respect to the ratio between contour axis lengths, an indication that the material can no longer maintain its original thermal property when it reaches its mechanical critical state. The full mechanical history in terms of contour axis length ratio representation shows similarity to the conventional stress-strain constitutive relation [3,21,22].

A more detailed phenomenological analysis can be performed with respect to the anisotropy indicator. The entire mechanical history represented in terms of λ is shown in Fig. 7(d). Referring to Table 1, first row, within the elastic regime, the absolute value of λ starts from 0 and increases rapidly while anisotropy begins to form and accumulate fast. P_{yy} becomes non-zero and increases under y-axis tensile loading while P_{zz} and P_{xx} fluctuate around 0 with much smaller magnitude. This results in variation of the denominator of λ from a small positive number, crossing over 0, to a negative number and occurs at ~5000 μm/m. The stress-conductivity tensor component (P_{yy}) behavior is consistent with elastic performance or the early stage of plastic deformation. In the second row, the sample gradually crossed over into severe plasticity. λ is negative and gradually increases to approach 0. In this regime, P_{yy} stops increasing and/or even begins to decrease; P_{xx} and P_{zz} are negative due to Poisson's deformation and their absolute values increase rapidly. This feature implies that k_{xx}, k_{yy} and k_{zz} all change considerably nonlinearly with respect to the increasing uniaxial loading. In the third row, λ slightly increases, crosses over 0, becomes positive but remains below 1. λ has both negative numerator and denominator, so that it varies in the range $1 > \lambda > 0$. This is due to the fact that P_{yy} continues to decrease and/or P_{xx} undergoes a dramatic change that is large enough to make the numerator of λ negative. The reason is the strong local deformation which occurs at the waist of the sample that leads to strong geometric and thermal parametric changes under the necking condition.

5. Conclusions

Photo-thermo-mechanical lock-in thermography (PTM-LIT) imaging was introduced and applied to the evaluation of the mechanical performance of a metallic aluminum alloy. It was shown that the anisotropic thermal-wave field due to a strained material coordinate satisfies the spatial equation of an ellipse. By fitting the isothermal phase contours with the ellipse equation, the change of the thermal conductivity tensor with local applied strain was quantified in terms of the ellipse axis length ratios under uniaxial tensile loading. A specific anisotropy indicator λ was introduced as an important criterion for mechanical strength evaluation. Small but measurable changes in the thermal conductivity tensor were extracted and the indicator exhibited large change from zero

(stress-free) to a large number (P_{yy} domination) within the elastic regime. A much larger scale of thermal conductivity anisotropy was observed when the sample was stretched to plasticity which corresponds to negative λ. A steep decrease of the λ-defining ratios was found when approaching the fracture point with a positive numerator. Within the elastic regime, a detailed analysis of material factors that affect the ellipse best-fitting results was presented and the change of the dominant conductivity tensor component was quantified by calculating the λ ratio. The PTM-LIT technique is totally based on non-contact instrumentation and compact mechanical rig configuration that allows simple remote operation without attaching strain gauges. The mechanical status is evaluated in terms of thermal anisotropy with the aid of isothermal contour fitting and the indicator parameter λ. This work enables the possibility of in-field implementation for a detailed *in-situ* extraction of anisotropic mechanical property images of stressed solids.

Acknowledgements

The authors are grateful to the Natural Sciences and Engineering Research Council of Canada (NSERC) for a Discovery grant to AM, and the Canada Research Chairs program. AM is also grateful to NSERC for a 2016 Engage Grant with Integran Technologies, Mississauga, ON. AM further gratefully acknowledges the Chinese Recruitment Program of Global Experts (Thousand Talents). He also acknowledges the Foundation for Innovative Research Groups of the National Natural Science Foundation of China (Grant No. 61421002). HH gratefully acknowledges the China Scholarship Council (CSC) program (No. 201406070045).

Appendix. Theory of linear coordinate transformation in a thermophysically anisotropic medium

Consider a thermal conductivity tensor in a thermally anisotropic medium (coordinate: 1,2,3). The thermal diffusion equation is:

$$\sum_{i,j}^{3} k_{ij}\frac{\partial^2 T}{\partial x_i \partial x_j} + Q(x_i;t) = \rho C \frac{\partial}{\partial t} T(x_i;t)\ \mathrm{i,j} = 1,2,3, \tag{1}$$

Applying a coordinate transformation to convert Eq. (1) into a canonical form [23]:

$$\begin{aligned} X &= x_1 + q_1 x_2 + q_2 x_3 \\ Y &= q_3 x_2 + q_4 x_3 \\ Z &= q_5 x_3 \end{aligned} \tag{2}$$

and using the chain rule for the differential operators:

$$\begin{aligned} \frac{\partial}{\partial x_1} &= \frac{\partial}{\partial X} \\ \frac{\partial}{\partial x_2} &= q_1\frac{\partial}{\partial X} + q_3\frac{\partial}{\partial Y} \\ \frac{\partial}{\partial x_3} &= q_2\frac{\partial}{\partial X} + q_4\frac{\partial}{\partial Y} + q_5\frac{\partial}{\partial Z} \end{aligned} \tag{3}$$

Now, assuming that the thermal conductivity tensor is symmetric, $k_{ij} = k_{ji}$, it can be shown that Eq. (1) can be simplified in the new coordinate (X, Y, Z) as:

$$\rho C \frac{\partial}{\partial t} T(X,Y,Z;t) = k_{33} q_5^2 \left(\frac{\partial^2 T}{\partial X^2} + \frac{\partial^2 T}{\partial Y^2} + \frac{\partial^2 T}{\partial Z^2}\right) + Q(X,Y,Z;t), \tag{4}$$

provided the coefficients in Eq. (2) satisfy:

$$\begin{aligned} &q_1 = (k_{23}k_{13} - k_{12}k_{33})\left(k_{22}k_{33} - k_{23}^2\right)^{-1}, q_2 = (k_{13}k_{22} - k_{12}k_{23})\left(k_{22}k_{33} - k_{23}^2\right)^{-1}, \\ &q_3 = \left(k_{22}k_{33} - k_{23}^2\right)^{-1}\left[\left(\left(k_{11}k_{22} - k_{12}^2\right)\right)k_{33}^2 + \left(2k_{13}k_{23}k_{12} - k_{11}k_{23}^2 - k_{13}^2 k_{22}\right)k_{33}\right]^{1/2} \\ &q_4 = -q_3 k_{23}k_{33}^{-1}, q_5 = q_3\left(k_{22}k_{33} - k_{23}^2\right)^{1/2}k_{33}^{-1} \end{aligned} \tag{5}$$

Considering the conductivity to be orthotropic, i.e. $k_{ij} = 0$ for $i \neq j$, then $q_1 = q_2 = q_4 = 0$, $q_3 = (k_{11}/k_{22})^{1/2}$, $q_5 = (k_{11}/k_{33})^{1/2}$.

References

[1] Teagle PR. The quality control and non-destructive evaluation of composite aerospace components. Composites 1983;14:115–28.
[2] Scott IG, Scala CM. A review of non-destructive testing of composite materials. NDT Int 1982;15:75–86.
[3] Huan H, Mandelis A, Liu L, Melnikov A. Non-destructive and non-contacting stress–strain characterization of aerospace metallic alloys using photo-thermo-mechanical radiometry. NDT E Int 2016;84:47–53.
[4] Huan H, Mandelis A, Liu L, Melnikov A. Evaluation of mechanical performance of NiCo nanocoated aerospace aluminum alloy using quantitative photo-thermo-mechanical radiometry as a non-contact strain gauge. NDT E Int 2017; 87:44–9.
[5] Mzali F, Albouchi F, Nasrallah SB, Petit D. Optimal experiment design and thermo-physical characterization of a plastically deformed solid. Inverse Probl Sci Eng 2009;17:335–45.
[6] Pron H, Bissieux C. 3-D thermal modelling applied to stress-induced anisotropy of thermal conductivity. Int J Therm Sci 2004;43:1161–9.
[7] Paoloni S, Tata ME, Scudieri F, Mercuri F, Marinelli M, Zammit U. IR thermography characterization of residual stress in plastically deformed metallic components. Appl Phys A 2010;98:461–5.
[8] Mandelis A. Photoacoustic, photothermal, and diffusion-wave sciences in the twenty-first century: triumphs of the past set the trends for the future. Int J Thermophys 2012;33:1776–7.
[9] Landau LD, Lifshitz EM, Theory of Elasticity Pergamon Press, Bristol; 1959. pp. 15–17, 119-122.
[10] Iravani MV, Nikoonahad M. Photothermal waves in anisotropic media. J Appl Phys 1987;62:4065–71.
[11] Quelin X, Perrin B, Louis G, Peretti P. Three-dimensional thermal-conductivity-tensor measurement of a polymer crystal by photothermal probe-beam deflection. Phys Rev B 1993;48:3677.

[12] Salazar A, Sánchez-Lavega A, Ocáriz A, Guitonny J, Pandey GC, Fournier D, et al. Thermal diffusivity of anisotropic materials by photothermal methods. J Appl Phys 1996;79:3984–93.
[13] Salazar A, Sánchez-Lavega A, Fernández J. Thermal diffusivity measurements on solids using collinear mirage detection. J Appl Phys 1993;74:1539–47.
[14] Balderas-López JA, Mandelis A. Self-normalized photothermal technique for accurate thermal diffusivity measurements in thick metal layers. Rev Sci Instrum 2003;74:5219–25.
[15] Garcia JA, Mandelis A, Farahbakhsh B, Lebowitz C, Harris I. Thermophysical properties of thermal sprayed coatings on carbon steel substrates by photothermal radiometry. Int J Thermophys 1999;20:1587–602.
[16] Munidasa M, Mandelis A, Ball M. Buried thermoplastic layer diagnostics by the use of combined frequency-domain and impulse response photo-thermo-mechanical radiometry. Rev Sci Instrum 1998;69:507–11.
[17] Muratikov KL, Glazov AL, Rose DN, Dumar JE. Photoacoustic effect in stressed elastic solids. J Appl Phys 2000;88:2948–55.
[18] Carlsaw HS, Jaeger JC. Conduction of heat in solids. 2nd Ed. Oxford: Clarendon Press; 1959. Sect. 1.18.
[19] Mandelis A. Diffusion-wave fields: mathematical methods and green functions. New York: Springer; 2001. chap. 4.
[20] Hughes DS, Kelly JL. Second-order elastic deformation of solids. Phys Rev 1953;92:1145–9.
[21] MacKenzie DS. Handbook of aluminum. In: Totten GE, MacKenzie DS, editors. Alloy production and materials manufacturing, vol. 2. Abingdon: Taylor & Francis Group; 2003. p. 396.
[22] Yiping Hu. Mechanics of material. In: Chinese. Chengdu: Sichuan University Press; 2010. p. 63–7.
[23] Hsieh M, Ma C. Analytical investigations for heat conduction problems in anisotropic thin-layer media with embedded heat sources. Int J Heat Mass Transf 2002;45:4117–32.